Room temperature quantum anomalous Hall insulator in honeycomb lattice, $RuCS_3$, with large magnetic anisotropy energy

Yong-Chun Zhao(赵永春)[1], Ming-Xin Zhu(朱铭鑫)[1], Sheng-Shi Li(李胜世)[2], and Ping Li(李萍)[1,†]

[1] *School of Physics and Technology, University of Jinan, Jinan* 250022, *China*
[2] *Institute of Spintronics, University of Jinan, Jinan* 250022, *China*

(Received 5 August 2022; revised manuscript received 22 October 2022; accepted manuscript online 17 November 2022)

The quantum anomalous Hall (QAH) effect has attracted enormous attention since it can induce topologically protected conducting edge states in an intrinsic insulating material. For practical quantum applications, the main obstacle is the non-existent room temperature QAH systems, especially with both large topological band gap and robust ferromagnetic order. Here, according to first-principles calculations, we predict the realization of the room temperature QAH effect in a two-dimensional (2D) honeycomb lattice, $RuCS_3$ with a non-zero Chern number of $C = 1$. Especially, the nontrivial topology band gap reaches up to 336 meV for $RuCS_3$. Moreover, we find that $RuCS_3$ has a large magnetic anisotropy energy (2.065 meV) and high Curie temperature (696 K). We further find that the non-trivial topological properties are robust against the biaxial strain. The robust topological and magnetic properties make $RuCS_3$ have great applications in room temperature spintronics and nanoelectronics.

Keywords: quantum anomalous Hall (QAH) effect, room temperature, magnetic anisotropy energy, topological properties, first-principles calculations

PACS: 73.20.At, 75.50.Gg, 75.70.Ak **DOI:** 10.1088/1674-1056/aca396

1. Introduction

Topological materials have attracted extensive attention because of their intriguing transport properties.[1–4] Especially, the quantum anomalous Hall (QAH) insulator, also called the Chern insulator, is a two-dimensional (2D) magnetic insulator with the non-zero Chern number and quantized Hall conductivity in the absence of an external magnetic field. The quantized conductivity is written as $\sigma_{xy} = C(e^2/h)$. The Chern number (C) is equal to the number of gapless chiral edge states along an edge of the finite width nanoribbon. These chiral edge states are robust against any impurity perturbations and topologically protected. Because of the novel non-trivial topological characteristics and desirable potential applications in designing low-energy spintronics and electronics, extensive theoretical research and experimental research have recently been carried out to find room temperature QAH insulators.[5–18] So far, the QAH effect has been experimentally reported in V/Cr-doped $(Bi,Sb)_2Te_3$ films at an extremely low temperature and the van der Waals-layered material $MnBi_2Te_4$ at 1.4 K.[19] On the other hand, the V/Cr-doped $(Bi,Sb)_2Te_3$ has the low carrier mobility by the disorder on account of the doped magnetic atoms, and has the weak magnetic coupling, which may be derived from the localized V/Cr-3d orbitals that scarcely overlap with the orbitals of the adjacent V/Cr atoms.

The problems of the small band gap and weak magnetic coupling can be overcome by importing 4d transition metal atoms that synchronously have more expanded d orbitals and stronger spin–orbital coupling (SOC). For practical applications, it is of significance to search for QAH insulator materials with huge magnetic anisotropy energy, large band gap, high carrier mobility, and simultaneously high Curie temperature (T_C).[4] Obviously, it would be meaningful to search for the high T_C QAH effect in ferromagnetic (FM) 4d transition metal materials.

In this work, we present a Dirac half metal in two-dimensional (2D), namely $RuCS_3$, by using first-principles calculations. Our research result shows that $RuCS_3$ has good mechanical stability and thermal stability, ferromagnetism, Curie temperature higher than room temperature, implying the possibility that the configuration and the ferromagnetic characteristic can be realized and observed experimentally in future. On the top of that, $RuCS_3$ has Dirac point which is fully spin-polarized near the Fermi level with a Fermi velocity as high as 1.92×10^5 m/s. The Dirac point is at point K in the Brillouin zone which is protected by vertical mirror symmetry. Considering SOC, the out-of-plane spin polarization destroys the vertical mirror symmetry. The band gap of $RuCS_3$ is 336 meV calculated by PBE+U. Further calculating of the edge states, Berry curvatures and Chern number show that the $RuCS_3$ is a QAH topological insulator. The $RuCS_3$ monolayer has broad application prospect in the field of spin electronic devices.

†Corresponding author. E-mail: ss_lip@ujn.edu.cn

© 2023 Chinese Physical Society and IOP Publishing Ltd

2. Computational methods

Based on the first principle of density functional theory (DFT), the calculation is performed by using the Vienna *ab initio* simulation package (VASP).[20,21] The Perdew–Burke–Ernzerhof (PBE)-type[22–24] generalized gradient approximation (GGA)[25,26] exchange–correlation functional is chosen, with the Hubbard term correction of $U = 3.0$ eV on the d-orbital of Ru to describe the strongly correlated interactions of transition metal elements.

For all calculations, the electron plane wave function is expanded up to cutoff energy of 500 eV. In terms of structure optimization, a $9 \times 9 \times 1$ Brillouin sampling grid is used to relax the original cell. In order to avoid the interaction between layers, a vacuum layer approximately 20 Å perpendicular to the plane is applied. The energy convergence value between two adjacent steps is 10^{-8} eV. When the Hellmann–Feynrnan force on each atom is less than or equal to 0.001 eV/Å, the structural relaxation ends. The phonon spectrum is calculated by using the density functional perturbation theory (DFPT) implemented in the PHONOPY code.[27] The *ab initio* molecular dynamics (AIMD) simulations are performed by using the Nose–Hoover algorithm in time steps of 1 fs at 300 K, in which a supercell of $3 \times 3 \times 1$ is used. An iterative Green's function method is utilized to calculate the edge density of states of the semi-infinite boundary of $RuCS_3$ based on the maximally localized Wannier functions (MLWFs) with considering SOC effects.

3. Results and discussion

3.1. Geometric structure and stability of $RuCS_3$ lattice

The geometric structure of the $RuCS_3$ monolayer is shown in Fig. 1(a). It can be seen that each unit cell of $RuCS_3$ contains two ruthenium (Ru) atoms, two carbon (C) atoms, and six sulfur (S) atoms. This configuration belongs to the space group (No. 162). The optimized lattice constants are $a = b = 5.58$ Å, and the calculations on the energy–strain relations, as plotted in Fig. 1(b), are also performed to confirm that the lattice constant is at the energy minimum. Each Ru atom has six neighboring S atoms, with the Ru–S bond length being 2.38 Å. And each C has three neighboring S atoms, with the C–S bond length being 1.84 Å. The ground state of $RuCS_3$ is spin-polarized, with a magnetic moment of 2 μ_B per the unit cell, which is 0.203 eV lower than the nonmagnetic configuration. In order to evaluate the stability of $RuCS_3$, the cohesive energy $E_C = (2E_{Ru} + 2E_C + 6E_S - E_{Ru2C2S6})/10 = 5.423$ eV/atom is calculated first, where E_{Ru}, E_C, E_S, and $E_{Ru2C2S6}$ are the energy of a single Ru, C, S atom, and a unit cell of the $RuCS_3$ monolayer respectively. The large cohesive energy shows the strong binding interaction and the possibility of experimental synthesis from elementary substances. The dynamic stability of $RuCS_3$ is evaluated as well. And the phonon dispersion spectrum plotted in Fig. 2(a) shows no imaginary frequency, which demonstrates the dynamic stability of free-standing $RuCS_3$. In addition, *ab-initio* molecular dynamics simulations at 300 K are performed by using a 3×3 super-cell in time steps of 1 fs. The energy evolution and the final configuration at the end of molecular dynamics simulations are plotted in Fig. 2(b), illustrating the good thermal dynamic stability.

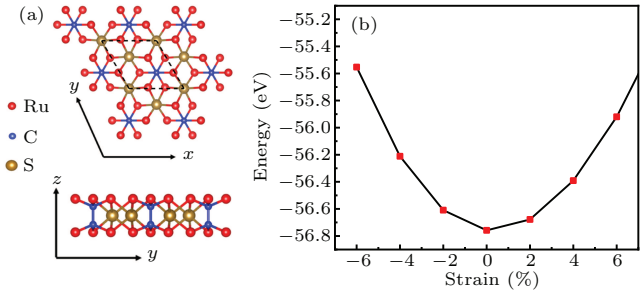


Fig. 1. (a) Top view and side view of lattice geometry of $RuCS_3$ monolayer and (b) curve of energy *versus* strain of $RuCS_3$.

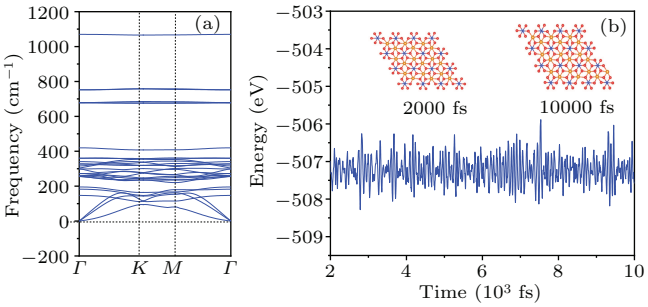


Fig. 2. (a) Calculated phonon spectrum. (b) Variations of energy for $RuCS_3$ lattice during MD simulations at temperature of 300 K, with inset illustrating optimized crystal structures of the $RuCS_3$ lattice at 2000 fs and 10000 fs.

3.2. Electronic band structures

In Figs. 3(a) and 3(b), the red lines and blue lines represent the spin-up and spin-down band structures, respectively. It can be seen that the energy of spin-up band and spin-down band are separated by 100% spin polarization. From Figs. 3(a), 3(b), and 4(a), without SOC, the spin-up bands have a band gap of 2.51 eV away from the Fermi level, while the spin-down band is conductive with zero band gap, and the two energy bands near the Fermi level intersect at the high symmetry point K to form a Dirac cone. A linear dispersion relationship is present at the intersection, with a Fermi velocity $v_F = 1.92 \times 10^5$ m/s and the effective mass of zero (at the same order of magnitude as graphene). The orbital components of the bands are shown in Fig. 3(c), and the Dirac cone components of the spin-down channel in the $RuCS_3$ are mainly derived from the $d_{x^2-y^2}$, d_{z^2}, d_{xz} orbitals of the Ru atom. Structural symmetry analysis reveals that, as shown in Fig. 4(c), there is a vertical mirror in the system which is Γ–K perpendicular to the 2D surface and protects the Dirac degeneracy

point on the high symmetry line of Γ–K. When considering SOC, as shown in Fig. 4(b), the Dirac point on K-point is broken with a band gap of about 336 meV. This result can also be explained by symmetry analysis: as mentioned earlier, the ground state of the system is a ferromagnetic state where the magnetic axis points outward, and the magnetic moment is contributed by the Ru atom. Since the spin is a pseudo-vector (axis vector), for the Γ–K vertical plane protecting the Dirac cone, the ferromagnetic spin arrangement perpendicular to the 2D plane destroys the mirror symmetry (Fig. 4(d)), resulting in the degeneracy release and band gap at the K point (which naturally also belongs to the Γ–K high symmetry line). Through the further analysis of structural symmetry, the protection mechanism of Dirac cone can be understood in depth.

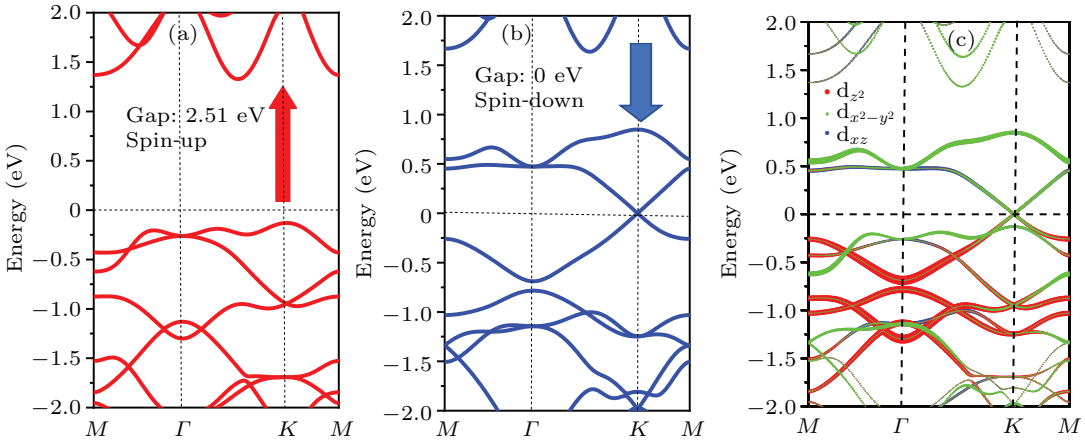


Fig. 3. (a), (b) Spin band structures of $RuCS_3$ without SOC and (c) orbit-resolved band structures of $RuCS_3$ without SOC.

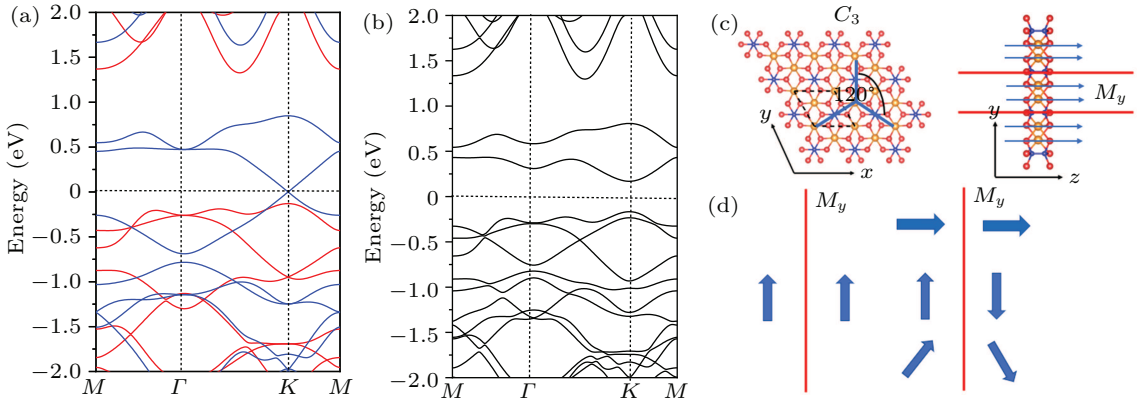


Fig. 4. Spin band structures of $RuCS_3$ (a) without and (b) with SOC. (c) Schematic diagram of structural symmetry: vertical mirror and in-plane C_3 which has rotational symmetry. (d) Left: Spin arrangement direction of magnetic atoms in $RuCS_3$; Right: Spin arrangement direction that satisfies the vertical mirror plane symmetry. All arrows indicate the spin direction.

3.3. Magnetic configurations and properties at finite temperature

According to the spin charge distribution and Barder analysis, we find the spin polarization comes mainly from Ru atom, and the local magnetic moment on each Ru atom is 1 μ_B (see Fig. S1 in supporting materials). In order to determine the magnetic configuration of $RuCS_3$, we propose the ferromagnetic (FM) configuration and antiferromagnetic (AFM) configuration in Fig. 6(a), and the results demonstrate the energy superiority of FM state.

Considering SOC effects, further calculations on magnetocrystalline anisotropy energy (MAE) are performed by rotating the spin in all directions. Table 1 reveals that the easy axis of magnetization is along the out-of-plane direction c (0 0 1) perpendicular to the layer plane, which is 2.065 meV lower in energy than those of in-plane spin polarizations along the direction a (1 0 0) and b (0 1 0), indicating the isotropy in the x–y plane. According to the symmetry of $RuCS_3$ monolayer, the angular dependence of MAE can be expressed as

$$\mathrm{MAE}(\theta) = K_1 \sin^2\theta + K_2 \sin^4\theta, \tag{1}$$

where K_1 and K_2 are the constants of anisotropy and (θ) is the polar angle in the spherical coordinates. Figures 5(a) and 5(b) show MAE as a function of the azimuth angle θ measured from the out-of-plane axis and the horizontal azimuth angle φ on in-plane axis, respectively. We find that the MAE reaches its minimum in the out-of-plane axis, indicating an out-of-plane magnetization direction show in Fig. 5(a). Fig-

ure 5(b) further illustrates that the MAE is isotropic in the x–y plane. By fitting the results of energy from first-principles calculations as presented in Fig. 5(c), the anisotropic constants are listed in Table 2. Clearly, K_1 is the predominant parameter, and $K_1 > 0$ suggests that the easy axis of magnetization is out-of-plane along the c axis. As the magnetic anisotropy of $RuCS_3$ is large, the Ising model should be employed to describe the interactions between local moments. The Hamiltonian of the system is defined as

$$H = -\sum_{ij} J_{ij} S_i S_j, \tag{2}$$

where $J_{i,j}$ represents the nearest neighbor coupling exchange constant, and $S_{i(j)}$ is the spin vector of Ru atom. The nearest neighbor coupling exchange constant J is defined as

$$E_{\mathrm{FM}} = E_0 - 3J|S|^2, \tag{3}$$

$$E_{\mathrm{AFM}} = E_0 + 3J|S|^2. \tag{4}$$

Thus

$$J = \frac{E_{\mathrm{AFM}} - E_{\mathrm{FM}}}{6|S|^2}. \tag{5}$$

We have $J = 151$ meV. The changes of magnetic moment and specific heat capacity with temperature are shown in Fig. 6(b), and the Curie temperature T_C is estimated at 696 K, indicating the possible magnetic application beyond room-temperature. As the distance between nearest Ru atoms is about 3.2 Å, the direct magnetic exchange interaction is supposed to be rather weak and the magnetic exchange mechanism can be understood by Ru–S–Ru super-exchange interactions. According to the Goodenough–Kanamori–Anderson's rule, the super-exchange interaction between magnetic atoms is usually ferromagnetic if the bridging angle is around 90°. In the case of $RuCS_3$, the bond angle among Ru–S–Ru is $\theta = 84.9°$. The angle is close to 90°, thus the magnetic coupling is expected to be ferromagnetic. We have confirmed this by constructing and analyzing magnetic structures.

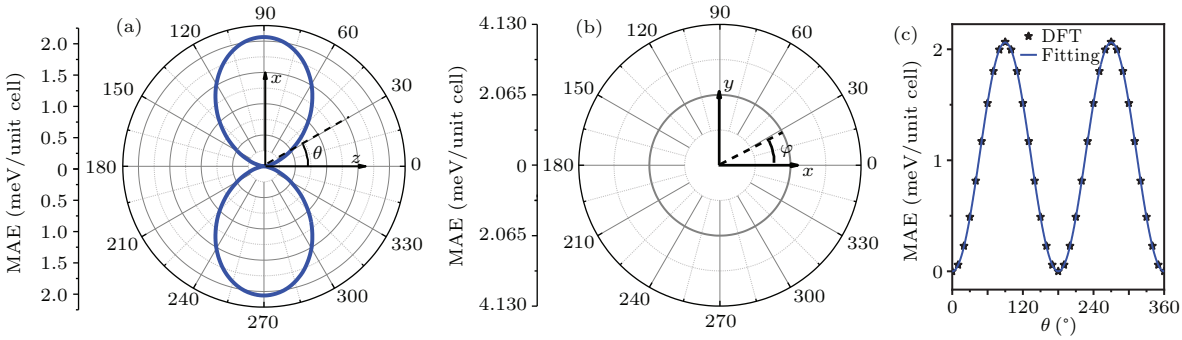


Fig. 5. Angular dependence of MAE within (a) x–z and (b) x–y planes. (c) Fitting results of MAE with x–z plane.

Table 1. MAE of $RuCS_3$ in some special directions (in units of meV).

(001)	(010)	(100)
0	2.065	2.065

Table 2. Constant of magnetic anisotropy K (in units of meV).

K_1	K_2
1.91	0.15

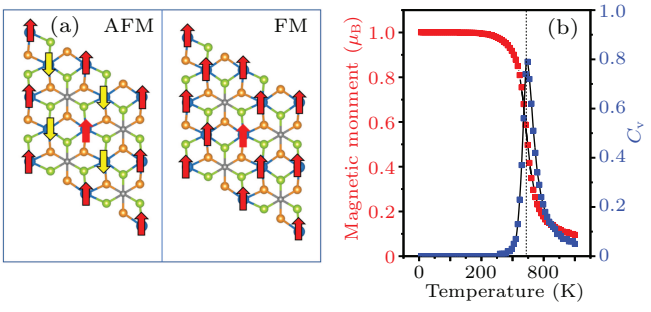


Fig. 6. (a) Schematics of different magnetic configurations: FM and AFM. (b) Monte Carlo simulations of time-dependent average magnetic moment and heat capacity (C_v) of $RuCS_3$.

3.4. QAH effect

The band gap in the system due to the introduction of soc action suggests that there may be a nontrivial edge state in the system. In order to confirm the nontrivial topological property of 2D $RuCS_3$, we first calculate its Chern number based on the Wannier charge center. The Chern number is calculated from

$$C = \frac{1}{2\pi} \sum_n \int_{\mathrm{BZ}} \mathrm{d}^2 k \Omega_n, \tag{6}$$

where BZ represents the integral over the Brillouin zone, and $\Omega(k)$ is the Berry curvature of all occupied bands and given by[28]

$$\Omega(k) = \sum_{n<E_{\mathrm{F}}} \sum_{m \neq n} 2\,\mathrm{Im} \frac{\langle \psi_{nk} | v_x | \psi_{mk} \rangle \langle \psi_{mk} | v_y | \psi_{nk} \rangle}{(\varepsilon_{mk} - \varepsilon_{nk})^2}, \tag{7}$$

where m and n are band indices, $\psi_{m(n)k}$ and $\varepsilon_{m(n)k}$ are the Bloch wavefunction and the corresponding eigen-energy of band $m(n)$, and $v_{x(y)}$ are the velocity operator. The results of Berry curvature in the whole BZ are shown in Fig. 7(c), and

clearly there are peaks of Berry curvature at all six K points. We then adjust its chemical potential μ with respect to E_F and calculate the anomalous Hall conductivity of the $RuCS_3$ monolayer σ_{xy} from $\sigma_{xy} = Ce^2/h$. As shown in Fig. 7(b), a quantized terrace of e^2/h inside the global band gap is clearly seen. The calculation of Chern number gives a result of $C = 1$, and the non-zero Chern number suggests that the gap opened by SOC is topological nontrivial, and indicates that $RuCS_3$ is a Chern insulator (quantum anomalous Hall insulator). This is further confirmed by the edge states plotted in Fig. 7(a). And only one nontrivial edge state connects the valence and conduction bands. Considering the possible effects of substrates in experiments, we calculate the band structure of $RuCS_3$ on the top of 2D ZnO monolayer (with a lattice mismatch of 1.1%) as shown in Fig. S2, and the result shows that the Diarc point can be preserved on the ZnO substrate.

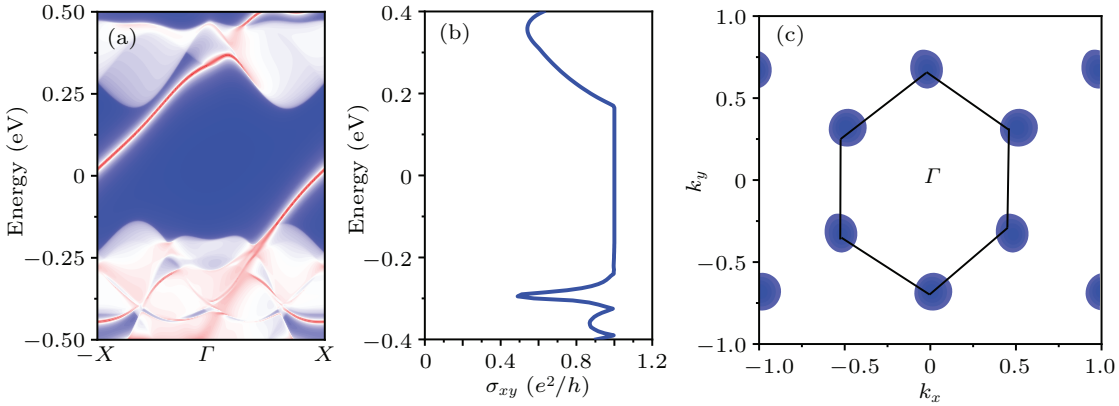


Fig. 7. (a) Chiral edge states of $RuCS_3$ monolayer, (b) integrated anomalous Hall conductance σ_{xy} in units of e^2/h, (c) Berry curvature with SOC in 2D momentum space.

3.5. Engineering of strain on electronic properties

We further check the robustness of the Dirac cone under biaxial strains. In-plane compressive strain and tensile strain up to ±6% are exerted on $RuCS_3$ monolayer, and the band structures are plotted in Fig. S3. It is found that the spin polarized Dirac cone is preserved under strains, suggesting their robustness against mechanical deformation and potential applications under in-plane pressures. Figures 8(a) and 8(b) show the evolution of E_{AFM}–E_{FM} energy and the direct gap E_g as a function of strain $\varepsilon = (a - a_0)/a_0$, where a (a_0) is the strained (equilibrium) lattice constant, since the strain generally changes the SOC-induced gap and the spin exchange constant J. Remarkably, the gap E_g increases with strain, and reaches 583 meV at the strain of 6% (Fig. S4). At the same time, figure 8(c) shows Fermi velocity also increases with the strain increasing, and arrives at 2.27×10^5 m/s with a strain of 6%.

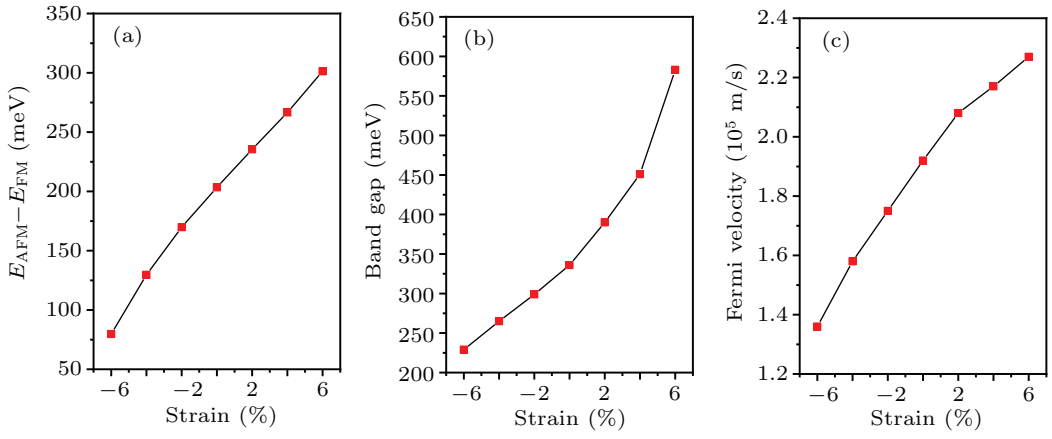


Fig. 8. Dependence of physical properties on the biaxial in-plane strain with $U = 3.0$ eV for Ru, with showing strain-dependent (a) exchange energy, (b) band gap, and (c) Fermi velocity.

3.6. Dependence of exchange energies on Hubbard U

As is well known, the exchange energy between the AFM state and the FM state in 2D FM material is sensitive to Hubbard U of transition-metal atoms. Thus, we check the band structures of $RuCS_3$ by employing various U values as shown in Fig. S5. In order to obtain the dependence of the exchange energy, the exchange coupling and the Curie temperature on Hubbard U, we perform GGA+U calculations by varying Hubbard U. Figure S6(a) gives the size dependence of ex-

change energy between the AFM and FM states on the Hubbard U value. We find that the energy difference between the FM state and the AFM state increase with the Hubbard U value increasing, which is important in forming high-temperature FM character. The switching coupling and the Curie temperature as a function of the Hubbard U are shown in Figs. S6(b) and S6(c). We find that they all increase with the Hubbard U value increasing.

Having systematically explored the properties of the $RuCS_3$ monolayer, we finally expand our research to XCS_3 (X = Ag, Cd, Co, Rh, Fe, Mn, Mo, Tc, Os) monolayers which share a similar structure to XCS_3. Figures S7–S15 show the corresponding geometric and band structures. The magnetic ground states of these monolayers are verified by comparing the energy of nonmagnetic, ferromagnetic, and antiferromagnetic configurations, as listed in Table S1. Additionally, the calculation results of band structure reveal that all monolayers show metallicity, except for $CoCS_3$, $FeCS_3$, and $RhCS_3$, which exhibits semiconducting properties. Hence, the presence of the Diarc cone in the $RuCS_3$ monolayer is due to the joint action of the crystal structure and electron configuration.

4. Conclusions and perspectives

In this work, we perform first-principles calculations on 2D high-temperature Dirac half metal $RuCS_3$ monolayer, and predict that it has a fully polarized Dirac point, together with various electronic and magnetic anisotropies. (i) The stability can be verified by the cohesive energy, phonon dispersion, molecular dynamics. (ii) The ground state of $RuCS_3$ is ferromagnetic and derived from the super-exchange interaction between Ru–S–Ru, mainly contributed by Ru atoms, and the magnetic moment on each Ru atom is 1 μ_B. The susceptibility to magnetization axis is vertically horizontal and has a strong magnetic anisotropy of 2.065 meV. The T_C estimated from MC simulations based on the Ising model is 696 K. (iii) A fully spin-polarized Dirac point appears in spin-down channel, leaving the other channel insulating with a gap of up to 2.51 eV. When considering SOC, the ferromagnetic spin arrangement perpendicular to the 2D plane destroys the mirror symmetry, resulting in the degeneracy release and band gap at the K point (which naturally also belongs to the Γ–K high symmetry line). The spin-down band structure opens a global band gap of about 336 meV. (iv) The intrinsic QAH effect of $RuCS_3$ is verified by Chern number ($C = 1$) and the chiral edge state. (v) The gap E_g increases with strain increasing, and arrives at 583 meV with a strain of 6%. At the same time, Fermi velocity also increases with strain increasing, and reaches 2.27×10^5 m/s with a strain of 6%. These out-standing properties of $RuCS_3$ indicate that it is a promising 2D material for the potential applications in designing energy efficient spintronic devices.

Acknowledgements

Project supported by the Natural Science Foundation of Shandong Province, China (Grant No. ZR2019MA041), the Taishan Scholar Project of Shandong Province, China (Grant No. ts20190939), the National Natural Science Foundation of China (Grant No. 62071200), and the Shandong Provincial Natural Science Foundation, China (Grant No. ZR2020QA052).

References

[1] Müchler L, Yan B, Casper F, Chadov S and Felser C 2013 *Springer Ser. Mater. Sci.* **182** 123
[2] Nagaosa N, Sinova J, Onoda S, MacDonald A H and Ong N P 2010 *Rev. Mod. Phys.* **82** 1539
[3] Qi X L and Zhang S C 2011 *Rev. Mod. Phys.* **83** 1
[4] Weng H, Yu R, Hu X, Dai X and Fang Z 2015 *Adv. Phys.* **64** 227
[5] Zhang S, Genov D A, Wang Y, Liu M and Zhang X 2008 *Phys. Rev. Lett.* **101** 047401
[6] Yu R, Zhang W, Zhang H J, Zhang S C, Dai X and Fang Z 2010 *Science* **329** 61
[7] Qiao Z, Yang S A, Feng W, Tse W K, Ding J, Yao Y, Wang J and Niu Q 2010 *Phys. Rev. B* **82** 161414
[8] Ding J, Qiao Z, Feng W, Yao Y and Niu Q 2011 *Phys. Rev. B* **84** 195444
[9] Ding J, Qiao Z, Feng W, *et al.* 2011 *Phys. Rev. B* **84** 195444
[10] Qiao Z, Jiang H, Li X, *et al.* 2012 *Phys. Rev. B* **85** 115439
[11] Ezawa M 2012 *Phys. Rev. Lett.* **109** 055502
[12] Garrity K F and Vanderbilt D 2013 *Phys. Rev. Lett.* **110** 116802
[13] Wang Z F, Liu Z and Liu F 2013 *Phys. Rev. Lett.* **110** 196801
[14] Liu C C, Zhou J J and Yao Y 2015 *Phys. Rev. B* **91** 165430
[15] Li P, Li X, Zhao W, Chen H, Chen M X, Guo Z X, Feng J, Gong X G and Macdonald A H 2017 *Nano Lett.* **17** 6195
[16] Sun Q and Kioussis N 2018 *Phys. Rev. B* **97** 1
[17] Li P 2019 *Phys. Chem. Chem. Phys.* **21** 6712
[18] Wang K, Zhang Y, Zhao W, Li P, Ding J W, Xie G F and Guo Z X 2019 *Phys. Chem. Chem. Phys.* **21** 9310
[19] Chang C Z, Zhang J, Feng X, Shen J, Zhang Z, Guo M, Li K, Ou Y, Wei P, Wang L L, Ji Z Q, Feng Y, Ji S, Chen X, Jia J, Dai X, Fang Z, Zhang S C, He K, Wang Y, Lu L, Ma X C and Xue Q K 2013 *Science* **340** 167
[20] Kresse G and Furthmüller J 1996 *Comput. Mater. Sci.* **6** 15
[21] Kresse G and Hafner J 1993 *Phys. Rev. B* **47** 558
[22] Langreth D C and Mehl M J 1983 *Phys. Rev. B* **28** 1809
[23] Perdew J P, Burke K and Ernzerhof M 1996 *Phys. Rev. Lett.* **77** 3865
[24] Joubert D 1999 *Phys. Rev. B* **59** 1758
[25] Becke A 1988 *Phys. Rev. A* **38** 3098
[26] Heyd J, Scuseria G E and Ernzerhof M 2003 *J. Chem. Phys.* **118** 8207
[27] Togo A, Oba F and Tanaka I 2008 *Phys. Rev. B* **78** 134106
[28] Yao Y and Fang Z 2005 *Phys. Rev. Lett.* **95** 156601